Astronomy
&
Astrophysics

Multi-wavelength bispectrum speckle interferometry of R Leo and comparison with Mira star models[⋆]

K.-H. Hofmann[1], Y. Balega[2], M. Scholz[3,4], and G. Weigelt[1]

[1] Max-Planck-Institut für Radioastronomie, Auf dem Hügel 69, 53121 Bonn, Germany
[2] Special Astrophysical Observatory, Nizhnij Arkhyz, Zelenchuk region, Karachai-Cherkesia, 357147, Russia
[3] Institut für Theoretische Astrophysik der Universität Heidelberg, Tiergartenstr. 15, 69121 Heidelberg, Germany
[4] Chatterton Department of Astronomy, School of Physics, University of Sydney NSW 2006, Australia

Abstract. We present diffraction-limited (30 mas resolution) bispectrum speckle interferometry of the Mira star R Leo with the 6 m SAO telescope. The speckle interferograms were recorded through narrow-band interference filters with centre wavelength/bandwidth of 673 nm/8 nm (strong TiO absorption band), 656 nm/10 nm, 699 nm/6 nm and 781 nm/14 nm (moderate TiO absorption), 754 nm/6 nm (weak TiO absorption), and 1045 nm/9 nm (continuum). The reconstructed images show that the average uniform-disk diameters of R Leo are 60.6 mas $\pm$ 3.0 mas at 656 nm, 75.6 mas $\pm$ 3.7 mas at 673 nm, 52.5 mas $\pm$ 2.5 mas at 699 nm, 48.7 mas $\pm$ 2.3 mas at 754 nm, 55.0 mas $\pm$ 2.7 mas at 781 nm, and 37.9 mas $\pm$ 4.0 mas at 1045 nm. In all six observed wavelength bands the shape of R Leo shows no significant asymmetry. We compare our observations with Mira star models and check the ability of monochromatic linear diameters for discriminating between model representations of the observed star. Monochromatic $\tau_\lambda = 1$ radii were derived from the observed visibilities by application of model-predicted center-to-limb variations of the intensity. Adopting the HIPPARCOS parallax we derived from the 1045 nm-observation a photospheric radius (Rosseland $\tau_{\mathrm{Ross}} = 1$ radius) of R Leo of 417 $R_\odot \pm 97\ R_\odot$ (19.2 mas $\pm$ 2.0 mas) indicating pulsation in the first-overtone mode. From *JHKL* photometry and the angular photospheric radius an effective temperature of 2590 ± 180 K at near maximum phase was obtained.

Key words. techniques: interferometric – methods: observational – stars: AGB and post-AGB – stars: imaging – stars: late-type – stars: variables: general – stars: individual: R Leo

1. Introduction

High-resolution interferometric observations of Mira stars allow the study of the size of the stellar disk, photospheric asymmetries, surface inhomogeneities, and the wavelength, pulsation phase and pulsation cycle dependence of the diameter (see, e.g., Pease 1931; Bonneau & Labeyrie 1973; Labeyrie et al. 1977; Bonneau et al. 1982; Karovska et al. 1991; Haniff et al. 1992; Quirrenbach et al. 1992; Wilson et al. 1992; Tuthill et al. 1994; Danchi et al. 1994; Haniff et al. 1995; Hofmann et al. 1995a; Weigelt et al. 1996; van Belle et al. 1996; Burns et al. 1998; Perrin et al. 1999; Hofmann et al. 2000a; Hofmann et al. 2000b; Weigelt et al. 2000). Theoretical studies (e.g. Watanabe & Kodaira 1979; Scholz 1985; Bessell et al. 1989; Bessell et al. 1996 = BSW96) show that accurate monochromatic diameter measurements can improve our understanding of

M giant atmospheres. Previous interferometric single-dish observations of R Leo at optical wavelengths were reported by Labeyrie et al. (1977), Tuthill et al. (1994, 1999) and Haniff et al. (1995). Di Giacomo et al. (1991) reported high-resolution lunar occultation observations of R Leo in the near infrared, Danchi et al. (1994) interferometric 11.5 μm measurements, Burns et al. (1998) observations at optical wavelengths with the COAST interferometer, and Perrin et al. (1999) *K*-band observations with the IOTA interferometer.

In this paper we present diffraction-limited 2-dimensional images of R Leo reconstructed by the bispectrum speckle interferometry method and comparisons of the observations with Mira star models.

2. Observations and data reduction

2.1. Observational parameters

The R Leo speckle interferograms were obtained with the Russian 6 m telescope at the Special Astrophysical

---

Table 1. Observational parameters.

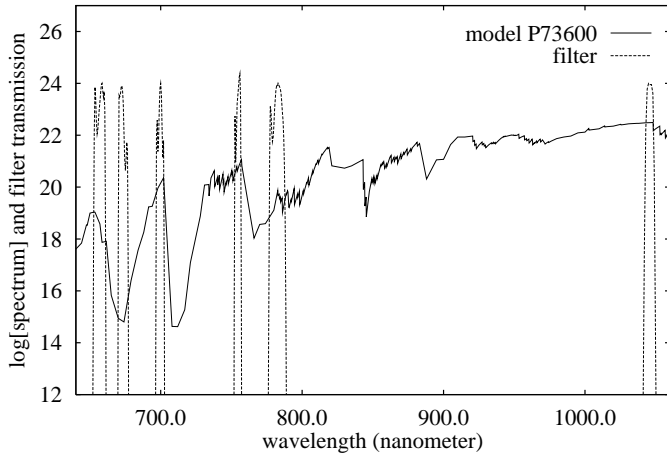| Data set	Epoche	Visual cycle and phase	Exposure time per frame	Photons/frame	Frames	FOV	Pixel size
656/10	1996.255	0 + 0.20	5 ms	53 800	516	2″40	4.69 mas
673/8	”	”	10 ms	23 400	2310	”	”
699/6	”	”	5 ms	71 100	130	”	”
754/6	”	”	”	94 500	200	”	”
781/14	”	”	”	120 600	1940	”	”
1045/9	”	”	70 ms	∼4 Mio	260	3″72	14.53 mas

Fig. 1. Typical model-predicted Mira star spectrum L_ν $(\mathrm{erg\,s^{-1}\,Hz^{-1}})$ (see BSW96) together with the transmission curves of our six interference filters (center wavelength (nm) / bandwidth (nm) 656/10, 673/8, 699/6, 754/6, 781/14 and 1045/9). The displayed spectrum is from the P model at phase 0.5 in cycle 1 (see Table 6).

Observatory on April 4, 1996 (see Table 1). The data were recorded through narrow-band interference filters with center wavelength (nm) / bandwidth (nm) of 656/10, 673/8, 699/6, 754/6, 781/14 and 1045/9 (filter width of the 6 filters at 10% transmission level: 12 nm, 9 nm, 8 nm, 6 nm, 16 nm, 13 nm; 1% level: 16 nm, 11 nm, 10 nm, 9 nm, 21 nm, 19 nm, respectively). Figure 1 shows the transmission curves of the filters. Due to the narrow bandwidth and the nearly rectangle-shaped transmission curve of our filters, specific regions of the molecular band structure of the Mira star spectrum can be selected which is important for sound physical interpretation (cf. Hofmann & Scholz 1998 = HS98; Hofmann et al. 1998 = HSW98). With these narrow-band filters quasi-monochromatic radii of R Leo can be measured in the strong TiO absorption band at 673 nm, at the moderate TiO absorption bands at 656 nm, 699 nm and 781 nm, in the weak TiO absorption band at 754 nm, and in the continuum at 1045 nm, suited for the comparison with predictions of Mira star models.

The observational parameters are listed in Table 1. Seeing was approximately 1″6. The plate scale error is ±1.5% and the error of detector orientation ±0.7° (derived from speckle observations of calibration binaries). The optical speckle interferograms were recorded with the speckle camera described by Baier & Weigelt (1983). The detector used was an image intensifier (gain 500 000, quantum efficiency: 9% at 600 nm, 8% at 700 nm, and less than 1% at 900 nm) coupled optically to a fast CCD camera (512^2 pixels/frame, frame rate 4 frames s^{-1}, digital correlated double sampling). The near-infrared speckle raw data (1045 nm continuum) were recorded with our NICMOS-3 camera.

2.2. Diffraction-limited images and visibilities

Diffraction-limited images were reconstructed from the speckle interferograms by the bispectrum speckle interferometry method (Weigelt 1977; Lohmann et al. 1983; Hofmann et al. 1995b). The visibilities of R Leo were determined with the speckle interferometry method (Labeyrie 1970). The speckle transfer function was derived from speckle interferograms of unresolved stars (HIC 49637, HIC 49669). The correct speckle transfer function was determined by comparison of the object-independent spectral ratio function (von der Lühe 1984) of object and reference star. The bispectrum of each frame consisted of ∼37 million elements.

Figure 2 presents the reconstructed diffraction-limited R Leo images and for comparison the 673 nm reconstruction of the unresolved star HIC 49637. These diffraction-limited images of R Leo (April 1996 at cycle+phase of 0 + 0.20) show no significant asymmetry in all six filters, i.e. in the continuum at 1.04 μm and in the TiO absorption bands showing the upper atmosphere. Note, however, the weak asymmetry reported by Lattanzi et al. (1997; November 1995 at cycle+phase of −1 + 0.71) and Tuthill et al. (1999; January 1992 at cycle+phase of −5 + 0.27, June 1993 at cycle+phase of −4 + 0.88). In contrast to R Leo, R Cas shows a strong asymmetry of its shape in all TiO absorption band filters (see Hofmann et al. 2000a).

Figure 3 shows the reconstructed diffraction-limited visibilities from which we derived the disk parameters of R Leo by fitting the following artificial (i.e. non-physical) center-to-limb variations (=CLV) of emitted intensity: uniform disk (UD), fully darkened disk (FDD) and Gaussian function (Gauss). Inspection of the 2-dimensional visibilities of R Leo in all six wavelength bands used yields axis ratios of the stellar disk ranging between 0.93 and 0.98. However, these axis ratios do not indicate any significant asymmetry of the shape of R Leo
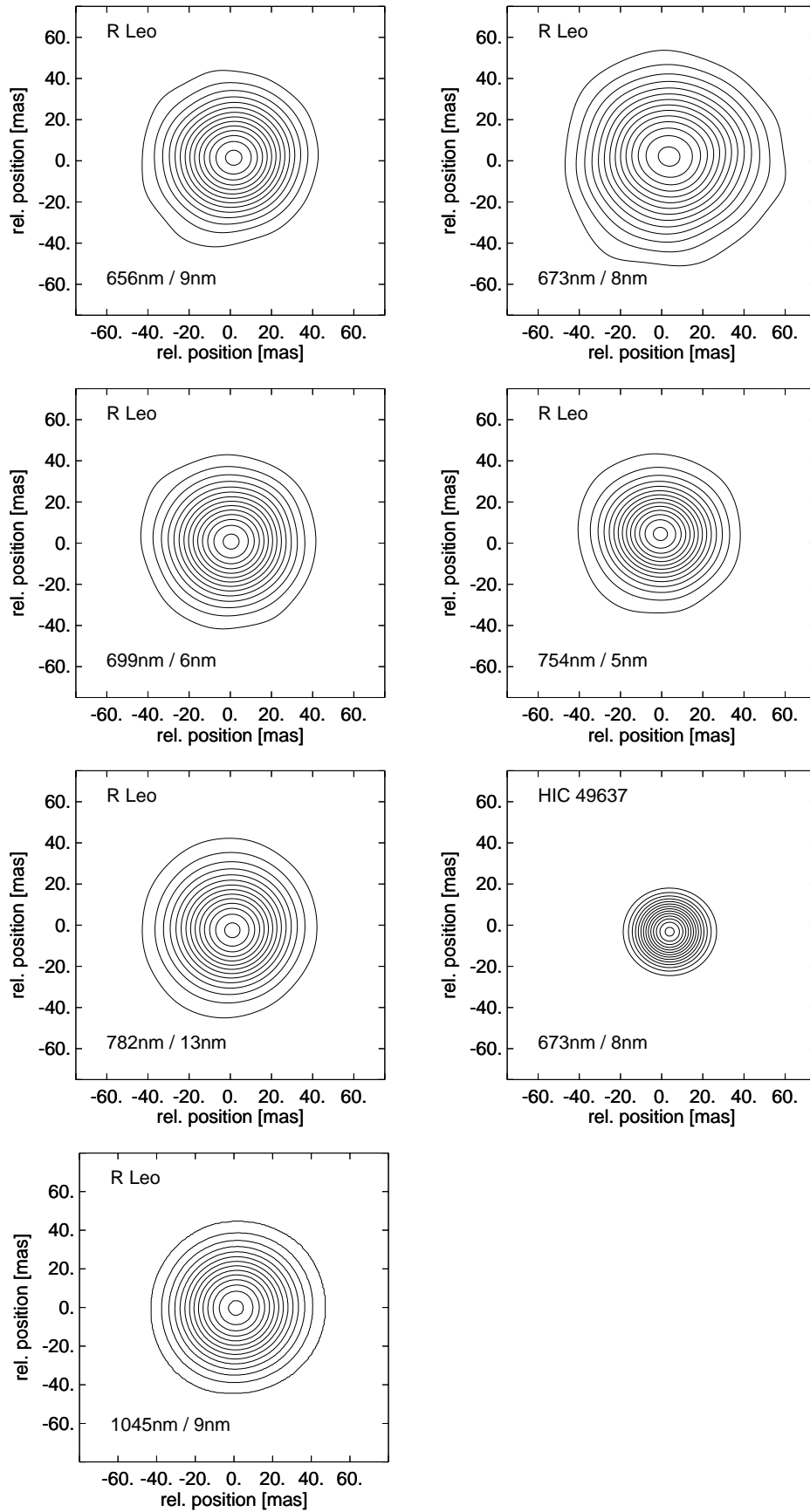
Fig. 2. Diffraction-limited bispectrum speckle interferometry images of R Leo at 656 nm, 673 nm, 699 nm, 754 nm, 781 nm and 1045 nm, and for comparison of the unresolved star HIC 49637 at 673 nm (the filter widths are described in Sect. 2.1). In each panel the contour levels are plotted from 7 to 98% of peak intensity in steps of 7%. North is at the top and east to the left.
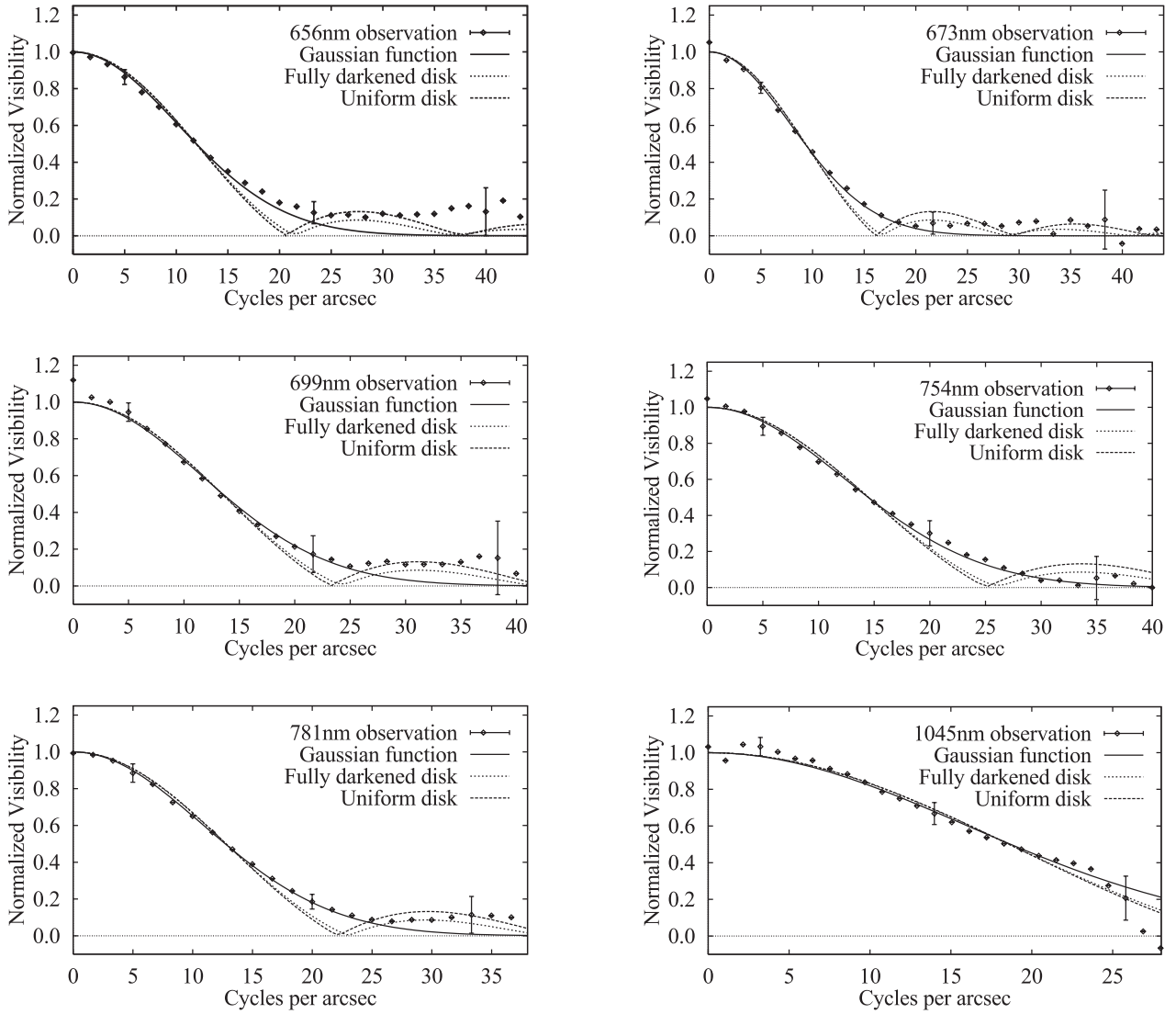
Fig. 3. Azimuthally averaged visibilities (diamonds) of R Leo and fitted visibilities of the artificial spherical symmetric UD, FDD and Gaussian CLV functions. From top left to right bottom: R Leo at 656 nm, 673 nm, 699 nm, 754 nm, 782 nm and 1045 nm. The solid line corresponds to the best fitting Gaussian CLV function, the dashed line to the best-fitting UD CLV function, and the small dashed line to the best-fitting FDD CLV function. The visibility data are plotted up to the telescope cut-off frequency (44.1, 43.2, 41.6, 38.6, 37.2, and 27.8 cycles/arcsec for 656 nm, 673 nm, 699 nm, 754 nm, 782 nm, and 1045 nm, respectively).

as the uncertainty of the axis ratios is approximately 10%. Hence, the disk parameters were derived from the azimuthally averaged 2-dimensional visibilities by fitting spherical symmetric CLVs.

In Fig. 3 the azimuthally averaged visibilities at 656 nm, 673 nm, 699 nm, 754 nm, 782 nm and 1045 nm together with the visibilities of the fitted spherical symmetric uniform disk and Gaussian functions are shown. Note, that the Gaussian function fits the reconstructed visibilities at optical wavelengths much better than FDD and UD, and that all three artificial CLVs fit the 1045 nm visibility equally well. Table 2 lists the fitted disk parameters of R Leo. Table 3 contains the diameters of Table 2 converted to linear radii (in solar radii $R_{\odot}$) using R Leo's HIPPARCOS parallax of 9.87 mas $\pm$ 2.07 mas (ESA 1997,

Whitelock & Feast 2000). Note, that Gaussian *FWHM* values are not directly comparable to diameter quantities.

Table 4 presents the ratios of the R Leo diameters at different wavelengths. We only list the FDD diameter ratios since the FDD approximation provides reasonable fits to the CLV in near-continuum filters and many other filters (HS98, HSW98), and since UD and Gaussian fits yield almost identical ratios. Note, however, that real diameter ratios can be different from those based on these artificial CLVs because, in particular, the shape of the physical CLV may be angle-dependent (e.g. occurrence of hot or cool spots). The UD diameter is approximately two times larger in the TiO absorption band head at 673 nm than in the 1045 nm continuum. The UD diameters at 656 nm, 699 nm and 781 nm (moderate TiO absorption band) are

Table 2. Disk parameters (diameter; *FWHM*) derived from fits of artificial spherical symmetric CLVs (UD, FDD; Gaussian) to the azimuthally averaged visibilities of R Leo.

Data set	Diameter/ $FWHM$ (mas)
UD	
656/10	60.6 ± 3.0
673/8	75.6 ± 3.7
699/6	52.5 ± 2.5
754/6	48.7 ± 2.3
781/14	55.0 ± 2.7
1045/9	37.9 ± 4.0
Gaussian	
656/10	38.1 ± 1.8
673/8	47.6 ± 2.3
699/6	32.7 ± 1.6
754/6	30.5 ± 1.5
781/14	34.6 ± 1.6
1045/9	23.6 ± 2.6
FDD	
656/10	68.3 ± 3.2
673/8	85.3 ± 4.0
699/6	59.0 ± 2.8
754/6	54.8 ± 2.6
781/14	62.1 ± 2.9
1045/9	42.7 ± 4.6

Table 3. Linear UD and FDD radii and Gaussian HWHM (in solar radii) based on the HIPPARCOS parallax of R Leo.

Data set	UD	Gaussian	FDD
656/10	660 ± 142	415 ± 89	744 ± 160
673/8	823 ± 177	518 ± 112	929 ± 200
699/6	572 ± 123	356 ± 77	642 ± 138
754/6	530 ± 114	332 ± 72	597 ± 128
781/14	599 ± 129	377 ± 81	676 ± 145
1045/9	413 ± 97	257 ± 61	465 ± 110

about 1.60, 1.38 and 1.46 times larger than at 1045 nm, respectively. The UD diameter at the weak TiO absorption band (754 nm) is about 1.28 times larger than at 1045 nm.

3. Comparison of the observations with Mira star models

In this section we compare our monochromatic radius observations with monochromatic radii predicted by Mira models. Since the wavelength dependence of the stellar radius sensitively depends on the model-predicted structure of the Mira atmosphere (Bessell et al. 1989, BSW96, HSW98), this comparison should give some hint whether any of the models is a fair representation of R Leo. We discuss the linear radii and the pulsation mode obtained by adopting R Leo's HIPPARCOS parallax and the

Table 4. Ratios of the R Leo diameters at different wavelengths (filters 1045 nm/9 nm, 781 nm/14 nm, 754 nm/6 nm, 699 nm/6 nm, 673 nm/8 nm and 656 nm/10 nm filter). The diameters used are derived from fits of the spherical symmetric fully darkened disk-model (FDD) to the reconstructed visibilities.

Feature		FDD diameter ratio
(754/6)	/ (1045/9)	1.28 ± 0.15
(699/6)	/ (1045/9)	1.38 ± 0.17
(781/14)	/ (1045/9)	1.46 ± 0.18
(656/10)	/ (1045/9)	1.60 ± 0.19
(673/8)	/ (1045/9)	2.00 ± 0.24
(699/6)	/ (754/6)	1.08 ± 0.08
(781/14)	/ (754/6)	1.14 ± 0.08
(656/10)	/ (754/6)	1.25 ± 0.09
(673/8)	/ (754/6)	1.56 ± 0.11
(781/14)	/ (699/6)	1.06 ± 0.07
(656/10)	/ (699/6)	1.16 ± 0.08
(673/8)	/ (699/6)	1.45 ± 0.10
(656/10)	/ (781/14)	1.09 ± 0.08
(673/8)	/ (781/14)	1.36 ± 0.10
(673/8)	/ (656/10)	1.25 ± 0.09

effective temperature derived from the 1045/9 measurement and the bolometric flux.

All Mira star models used in this paper are from BSW96 (D and E series) and from HSW98 (P, M and O series). They are meant as possible representations of the prototype Mira variable o Ceti, and hence have periods P very close to the 332 day period of this star; they differ in pulsation mode, assumed mass M and assumed luminosity L; and the BSW96 models differ from the (more advanced) HSW98 models with respect to the pulsation modelling technique. Solar abundances were assumed for all models. The five models represent stars pulsating in the fundamental mode (f; D, P and M models) or in the first-overtone mode (o; E and O models). Table 5 lists the properties of these Mira model series (R_p = Rosseland radius, i.e., distance from the non-pulsating "parent star's" center at which the Rosseland optical depth τ_Ross equals unity; $T_\mathrm{eff} \propto (L/R_\mathrm{p}^2)^{1/4}$ = effective temperature). We compare predictions of these models at different phases and cycles with our observations (Table 6; arbitrary numbering of model cycles). The correlation of bolometric model phases with visual phases was taken from Lockwood & Wing (1971) and Lockwood (1972) who discuss the observed light curves of Mira variables in their 104 filter (1035 nm/13 nm) which closely matches the bolometric light curve.

In this paper we use the conventional stellar radius definition where the monochromatic radius R_λ of a star at wavelength λ is given by the distance from the star's center at which the optical depth equals unity ($\tau_\lambda = 1$). In analogy, the photospheric stellar radius R is given by the distance from the star's center at which the Rosseland

Table 5. Properties of Mira model series (see text).

Series	Mode	P/day	$M/M_\odot$	$L/L_\odot$	$R_{\rm p}/R_\odot$	$T_{\rm eff}$
D	f	330	1.0	3470	236	2900
E	o	328	1.0	6310	366	2700
P	f	332	1.0	3470	241	2860
M	f	332	1.2	3470	260	2750
O	o	320	2.0	5830	503	2250

Table 6. Link between the 27 abscissa values (model-phase combinations m) in Figs. 6, 7, 9 and 10, and the models. Additionally the variability phase $\phi_{\rm vis}$, the Rosseland radius R and the 1045 nm radius $R_{\rm 1045nm}$ in units of the parent star radius $R_{\rm p}$, and the effective temperature $T_{\rm eff}(R)$ associated to the Rosseland radius are given.

Model	cycle+$\phi_{\rm vis}$	$R/R_{\rm p}$	$R_{1045}/R_{\rm p}$	$T_{\rm eff}(R)$	Abscissa
D27360	0 + 0.8	0.90	0.90	3050	1
D27520	1 + 0.0	1.04	1.04	3020	2
D27600	1 + 0.2	1.09	1.10	3010	3
D27760	1 + 0.5	0.91	0.90	2710	4
D28320	1 + 0.8	0.90	0.90	3050	5
D28760	2 + 0.0	1.04	1.05	3030	6
D28847	2 + 0.2	1.09	1.09	3000	7
D28960	2 + 0.5	0.91	0.90	2690	8
E8300	0 + 0.83	1.16	1.07	2330	9
E8380	1 + 0.0	1.09	1.09	2620	10
E8460	1 + 0.1	1.12	1.11	2760	11
E8560	1 + 0.21	1.17	1.15	2610	12
P71800	0 + 0.5	1.20	0.90	2160	13
P73200	1 + 0.0	1.03	1.04	3130	14
P73600	1 + 0.5	1.49	0.85	1930	15
P74200	2 + 0.0	1.04	1.04	3060	16
P74600	2 + 0.5	1.17	0.91	2200	17
P75800	3 + 0.0	1.13	1.14	3060	18
P76200	3 + 0.5	1.13	0.81	2270	19
P77000	4 + 0.0	1.17	1.16	2870	20
M96400	0 + 0.5	0.93	0.84	2310	21
M97600	1 + 0.0	1.19	1.18	2750	22
M97800	1 + 0.5	0.88	0.83	2460	23
M98800	2 + 0.0	1.23	1.20	2650	24
O64210	0 + 0.5	1.12	1.00	2050	25
O64530	0 + 0.8	0.93	0.91	2150	26
O64700	1 + 0.0	1.05	1.01	2310	27
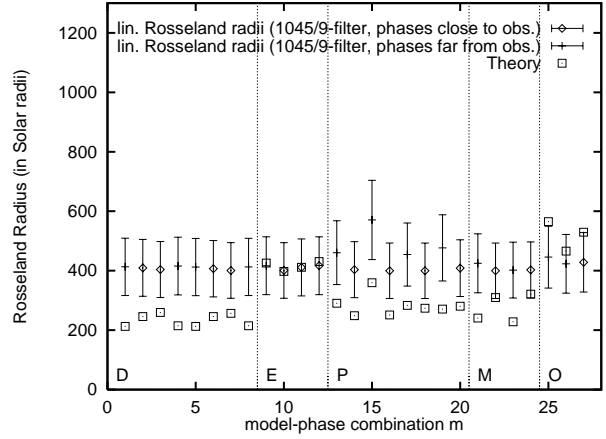
Fig. 4. Linear Rosseland observed and model radii. The observed linear Rosseland radii are based on the 1045/9 measurements for each model/phase combination; the model radii are calculated for the transmission curve of each filter used; Table 6 gives the link between the abscissa values and the models and their phases.

optical depth equals unity ($\tau_{\rm Ross} = 1$). This radius has the advantage of agreeing well (see Table 6 and the discussion in HSW98 for deviations sometimes occurring in very cool stars) with measurable near-infrared continuum radii and with the standard boundary radius of pulsation models with parameter $T_{\rm eff} \propto (L/R^2)^{1/4}$.

For each of our six filters (656/10, 673/8, 699/6, 754/6, 781/14 and 1045/9) we calculated the theoretical CLVs corresponding to the above mentioned five Mira models at different phases and cycles. The stellar radius for filter transmission f_λ is the intensity and filter weighted radius $R_{\rm f} = \int R_\lambda I_\lambda f_\lambda \, {\rm d}\lambda / \int I_\lambda f_\lambda \, {\rm d}\lambda$ which we call stellar filter radius $R_{\rm f}$ after the definition of Scholz & Takeda (1987). In this equation R_λ denotes the above monochromatic $\tau_\lambda = 1$ radius, I_λ the central intensity spectrum and f_λ the transmission of the filter. Owing to the chosen positions and narrow widths of our filters f, the $R_{\rm f}$ radii are almost monochromatic $\tau_\lambda = 1$ radii if the molecular line structure of the TiO bands is neglected.

The observed angular stellar filter radius $R_{\rm f,m}^{\rm a}$ of R Leo corresponding to a certain filter f and model-phase combination m, was derived by a least-squares fit between the azimuthally averaged measured visibility and the visibility of the corresponding theoretical CLV. For a detailed description of the visibility fitting procedure we refer to HS98.

In the following subsections we apply CLVs predicted from all five models at phases both near our R Leo observations (phase 0.20) and, for comparison, also at other phases.

3.1. Comparison of linear observed and model radii

Since R Leo is located in our neighborhood, the radii of the Mira star can be directly compared with the predictions of Mira star models. Linear stellar R Leo radii
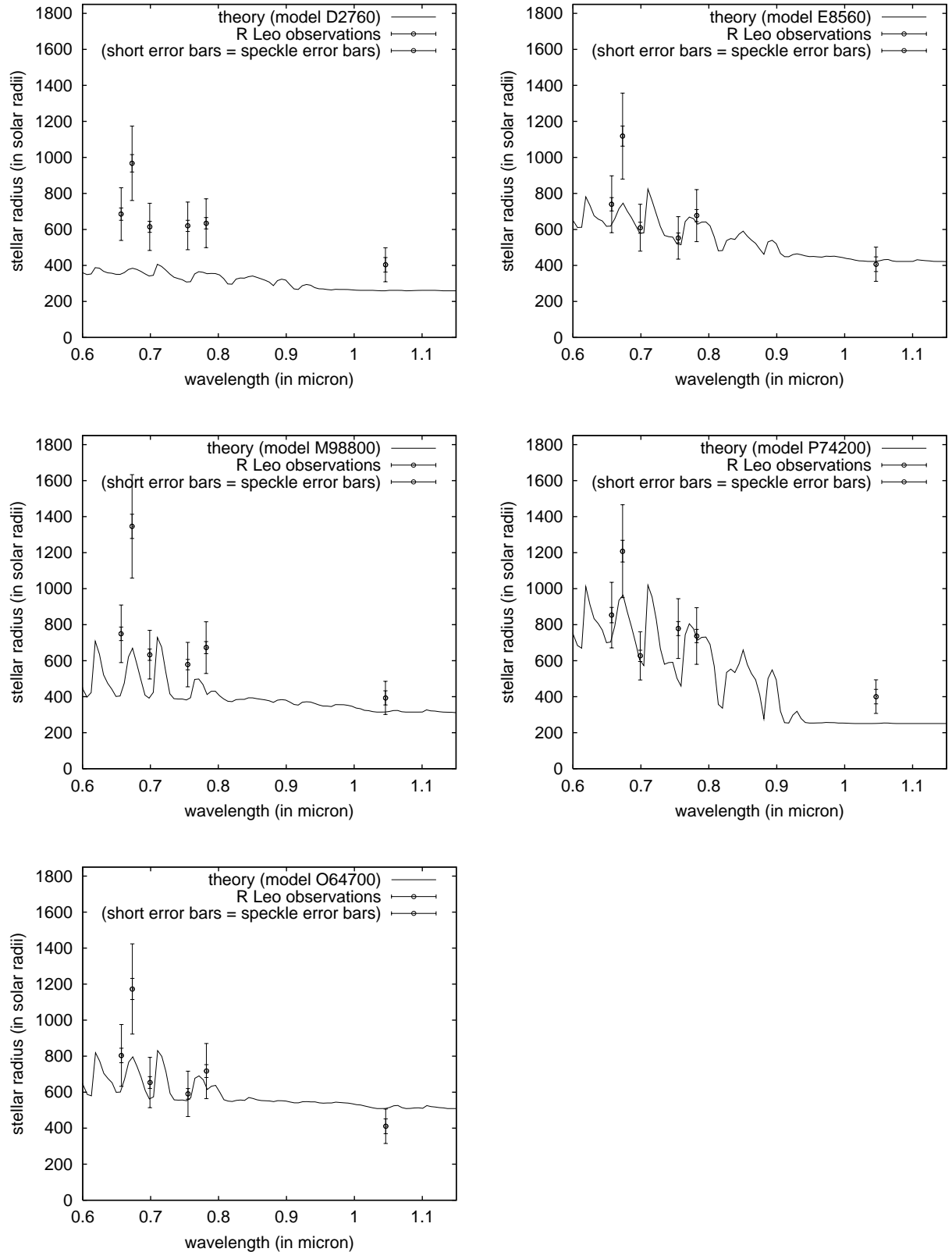
Fig. 5. Linear observed and model stellar filter radii R_f versus λ for all five models and phases close to our observations. The linear observed stellar filter radii R_f are derived from the measured visibility by using the visibilities of the model CLVs as fit functions, as described in the text. The plotted model stellar filter radius curve $R_f(\lambda)$ is derived from the monochromatic one by convolution with a rectangular-shaped function with a bandwidth of 6 nm (=bandwidth of our optical filters with the narrowest width). For each measurement two different symmetric error bars are plotted. The larger error bars contain both errors, the parallax error and also the speckle error. The smaller error bars (inner error bars) contain only the speckle error.

can be obtained if we use its HIPPARCOS parallax of 9.87 ± 2.07 mas (ESA 1997, Whitelock & Feast 2000; see discussion in this paper on the parallax errors in the case of stars with large extended shapes).

The 1045 nm model CLV visibility was fitted to the measured 1045 nm visibility of R Leo yielding the linear monochromatic $\tau_\lambda = 1$ radius R_{1045} and, as predicted by the specific model, the associated linear Rosseland radius R (Fig. 4). We see that the derived linear Rosseland radius values are nearly the same for all model-phase combinations, that is they depend very little on differences of CLVs of our models. The average measured R_{1045} radius is $395 \pm 92 \, R_\odot$ (18.2 ± 1.9 mas), and the average Rosseland radius is $423 \pm 99 \, R_\odot$ (19.4 ± 2.0 mas) (average over all model-phase combinations). The Rosseland radii of the E model series at all available phases (0.83, 1.0, 1.1, 1.21), of the M model series at near-maximum phases (1.0, 2.0), and of the O model at near-maximum phases (0.8, 1.0) are very close or close (within the error bars) to the Rosseland radii derived from the measured 1045 nm visibility at phase 0.20. All other model-phase combinations yield large differences (larger than the error bars).

The 1045 nm continuum model radius R_{1045} and the Rosseland model radius R averaged over all available E model phases is $404 \, R_\odot$ and $416 \, R_\odot$, respectively, and the measured value (using the E model CLVs) is $399 \pm 93 \, R_\odot$ and $411 \pm 96 \, R_\odot$, respectively. The E model at phase 1.21 (closest to our observed phase 0.20) has $R_{1045} = 420 \, R_\odot$ ($R = 431 \, R_\odot$). and data reduction by means of this CLV yields for R Leo the observed value of $R_{1045} = 407 \pm 95 \, R_\odot$ ($R = 417 \pm 97 \, R_\odot$). Hence, the difference between model and star is smaller than the error bar. Figure 5 presents all linear observed and model stellar filter radii R_f as a function of wavelength for all five models and phases close to our observations (in the case of model series with several cycles the best fitting model is shown).

In Fig. 6, we compare our observed linear stellar filter radii with the model radii of all 27 model-phase combinations m. Clearly the three fundamental-mode model stars are systematically too small (by ~20 to 50%), whereas most model radii of the overtone E and O series coincide within the error bars with the measured values. We see that the TiO forming layers of the Mira atmosphere may extend as far as 4 to 6 AU from the star's center. We also see from the figure that the model atmospheres are systematically more compact than the observed Mira atmosphere, i.e. the distance-independent ratio $(R_{strong-TiO} - R_{continuum})/R_{continuum}$ is too small in the here considered models (see Appendix for details).

3.2. Pulsation mode

After the period-radius relation of Miras from Feast (1996) a fundamental mode pulsator with a period of 310 days (R Leo) and with a mass ranging between 1.0 and 1.5 $M_\odot$ should have a linear photospheric radius ranging from $220-270 \, R_\odot$, and a first overtone pulsator

should have a linear photospheric radius ranging from $390-450 \, R_\odot$. Therefore, the measured linear Rosseland radius of $417 \, R_\odot \pm 97 \, R_\odot$ (derived from the 1045 nm-visibility measurement and the E-model at phase close to our observation) places R Leo among the first-overtone pulsators. The question why the period-radius relation of M-type Miras indicates first-overtone pulsation whereas MACHO observations (Wood et al. 1999) and pulsation velocities (Scholz & Wood 2000) favor fundamental mode pulsation, remains open.

3.3. Effective temperature

Effective temperatures of R Leo were derived from its angular Rosseland radii R_m^a (derived from the 1045/9-observation with all 27 above discussed models) and its bolometric flux using the relation $T_{eff} = 2341$ K $\times (F_{bol}/\Phi^2)^{1/4}$ where F_{bol} is the apparent bolometric flux in units of 10^{-8} erg cm^{-2} s^{-1} and $\Phi = 2 \, R_m^a$ is the apparent angular photospheric diameter in mas. Figure 7 (top) displays the angular Rosseland radii obtained from the 1045/9 observation by fitting all 27 theoretical model-phase CLV visibilities to the measured 1045/9 visibility. The average measured angular Rosseland radius is 19.4 mas (average over all model-phase combinations). Figure 7 (top) also shows that inaccuracies caused by adopting incorrect continuum limb-darkening from inadequate models rarely exceed ~10% (i.e. 5% in T_{eff}).

For cool stars such as LPV's, where most of the luminosity is emitted at near-infrared wavelengths, a convenient method for calculating bolometric magnitudes is to use a blackbody function to interpolate between photometric measurements in the J, H, K and L bands. For estimating the bolometric flux we have used $JHKL$-flux measurements from P. Whitelock's (1997, private communication) R Leo observations of April 6, 1996. These observations were carried out at nearly the same variability phase (0.20) and cycle as our 1045/9 observation of April 4, 1996. The bolometric magnitude of R Leo, calculated by P. Whitelock (1997, private communication) yields $m_{bol} = 0.24 \pm 0.20$ and, assuming that a zero magnitude star has a flux of 2795×10^{-8} erg cm^{-2} s^{-1}, yields $F_{bol} = (2240.69 \pm 412.30) \times 10^{-8}$ erg cm^{-2} s^{-1}. As a by-product we determined the luminosity of R Leo near maximum phase 0.20 from its bolometric magnitude and HIPPARCOS parallax to $6540 \pm 3010 \, L_\odot$, which is close to the near-maximum luminosity of the E and O model series (BSW96, HSW98).

Figure 7 (bottom) presents T_{eff} values derived for each of the 27 model-phase combinations from the bolometric flux and the angular Rosseland radii R_m^a measured at near-maximum phase 0.20. Fortunately, this value depends little on the model-phase combination CLV and is about 2590 ± 180 K (average over all model-phase combinations). The T_{eff} values of the E model series at all near-maximum phases (1.0, 1.1, 1.21) and of the M model series at all near-maximum phases (1.0, 2.0) are very close
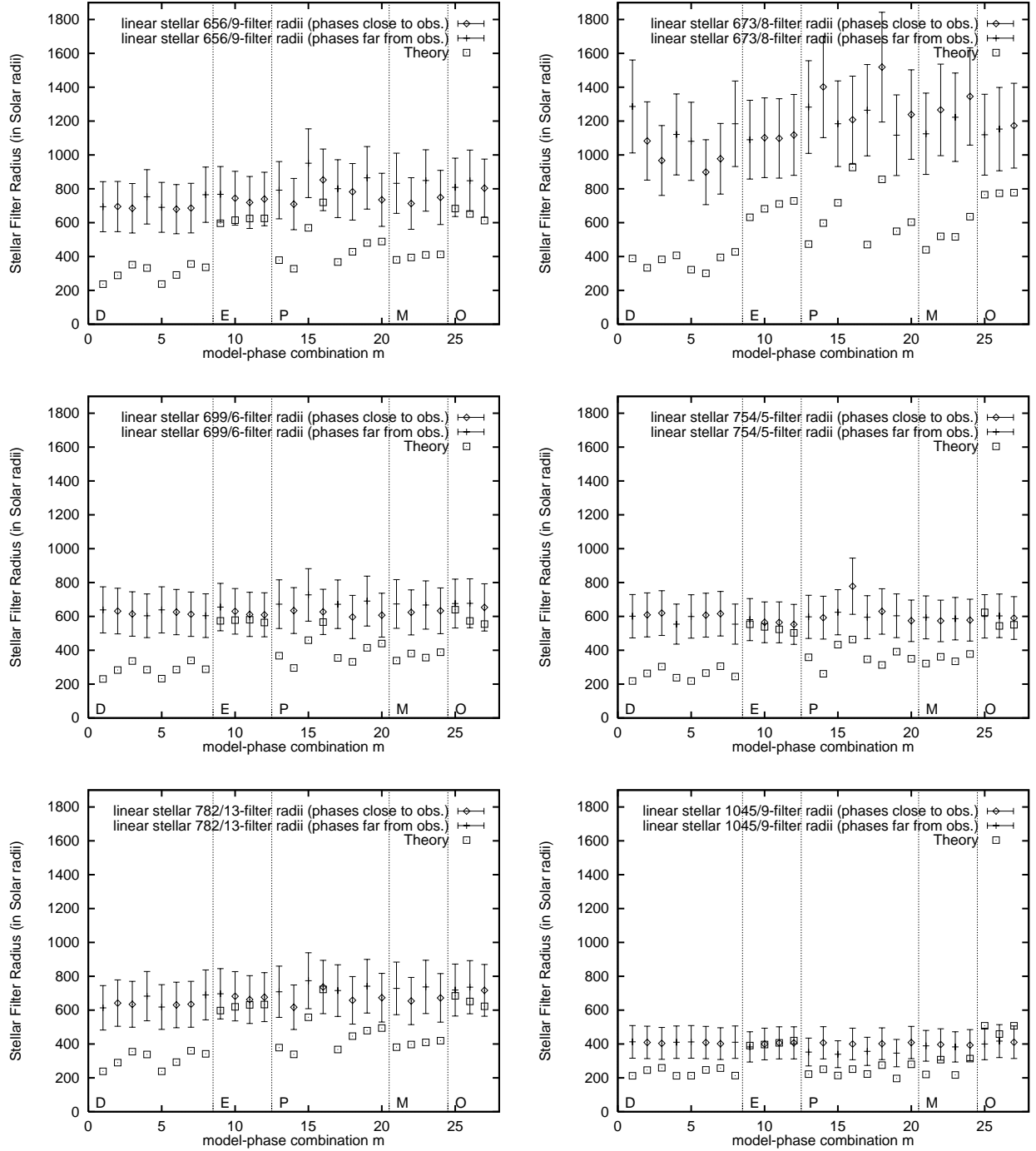
Fig. 6. Linear observed and model stellar filter radii R_f for all 27 model-phase combinations m. The stellar filter radii R_f are given for the six filters 656/9 (top left), 673/8 (top right), 699/6 (middle left), 754/5 (middle right), 782/13 (bottom left), and 1045/9 (bottom right). Table 6 gives the link between the abscissa values and the models and their phases. The large error bars of $\sim$20% are basically due to the parallax error; the speckle measurements with the optical filters have error bars of $\sim$5%, and with the near infrared filter 1045/9 $\sim$ 10% (diamonds: observations reduced with model CLVs with phases close to the phase of the observation; crosses: observations reduced with model CLVs with phases far from the phase of the observation; squares: model radii calculated for the transmission curve of each filter used).

(within the error bars) to the $T_{\rm eff}$ values derived from the 1045 nm visibility observation and the *JHKL* photometric measurement performed at the near-maximum phase 0.20. All other models (i.e. D, P and O) yield at all available near-maximum phases large differences between

theoretical and measured $T_{\rm eff}$ values. The closest E model with phase 1.21 has an effective temperature of 2610 K. Application of its CLV and $m_{\rm bol} = 0.24 \pm 0.20$ (measured at phase $\sim$0.20) to our 1045/9 observation yields for R Leo an angular Rosseland radius of 19.1 mas $\pm$ 2.0 mas and an
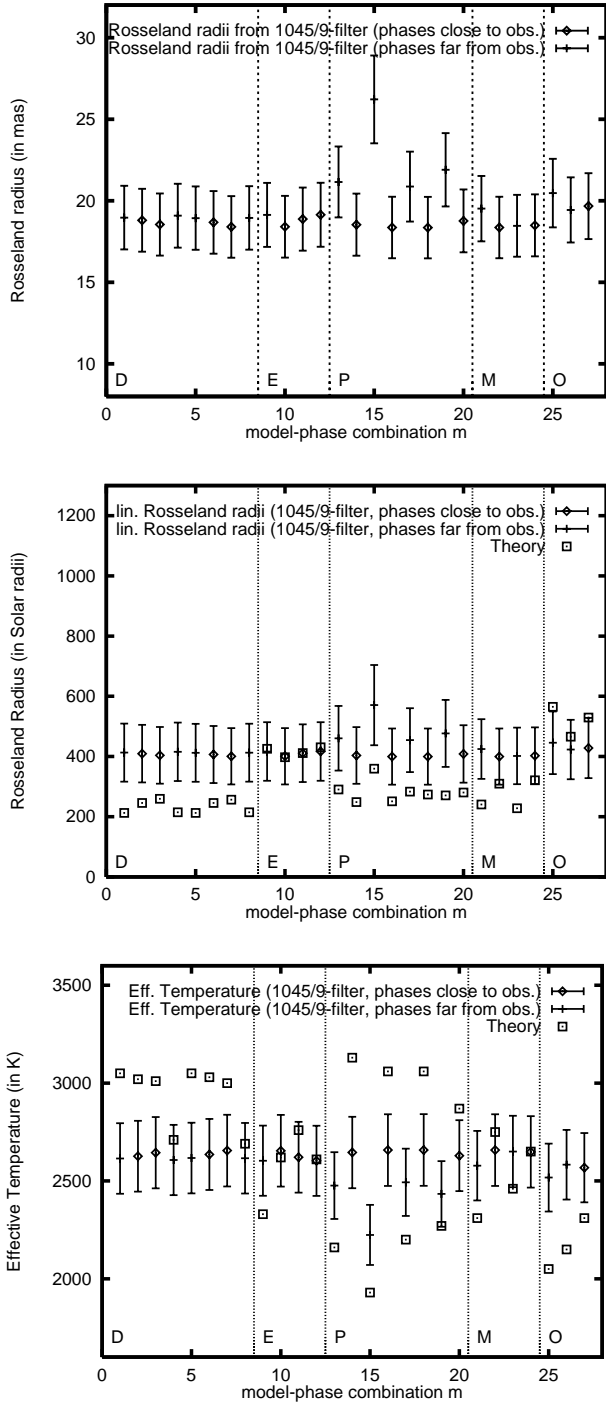
effective temperature of 2600 K ± 180 K. The average theoretical effective temperature of all near-maximum phases (1.0, 2.0) of the M model is 2700 K. The average measured effective temperature derived from the 1045/9 observation by application of the M model CLVs at the near-maximum phases 1.0 and 2.0 has a value of 2650 K ± 180 K.

4. Discussion and conclusion

From our speckle observations of R Leo at near maximum phase (phase 0.20) we derived UD diameters of

- 75.6 ± 3.7 mas at the strong TiO absorption band (673 nm/8 nm);
- 60.6 ± 3.0 mas, 52.5 ± 2.5 mas and 55.0 ± 2.7 mas at the moderate TiO absorption bands (656 nm/10 nm, 699 nm/6 nm and 781 nm/14 nm);
- 48.7 ± 2.3 mas at the weak TiO absorption band (754 nm/6 nm); and
- 37.9 ± 4.0 mas in the continuum at 1.04 μm (1045 nm/9 nm).

R Leo shows no significant asymmetry of its shape in all bands observed, i.e. in the continuum at 1.04 μm and in the TiO absorption bands showing the upper atmosphere (see Sect. 2.2). Contrary to R Leo, R Cas shows a significant asymmetry of its shape in all TiO absorption band filters (Weigelt et al. 1996; Hofmann et al. 2000a). On the other hand Lattanzi et al. (1997; November 1995 at cycle+phase of $-1 + 0.71$) and Tuthill et al. (1999; January 1992 at cycle+phase of $-5 + 0.27$, June 1993 at cycle+phase of $-4 + 0.88$) detected a weak asymmetry of the shape of R Leo, too.

Tuthill et al. (1994) derived UD diameters of 45 ± 2.0 mas and 43 ± 2.0 mas at 833 nm/41 nm and 902 nm/50 nm, respectively and derived Rosseland diameters of 37.4 ± 2.0 mas and 39.0 ± 2.0 mas, respectively. These measurements agree well with our angular Rosseland diameter of 38.4 ± 4.0 mas at phase 0.20 (April 4, 1996). Haniff et al. (1995) reported on R Leo observations through their 700 nm/10 nm filter comparable to our 699 nm/6 nm filter. They derived an UD diameter of 64.2 ± 5.7 mas at cycle+phase of $-4 + 0.88$ which is approximately 20% larger than our near-maximum phase (0.20) 699 nm/6 nm UD diameter of 52.5 ± 2.5 mas. This difference might be explained by UD diameter variations with the variability phase reported by Burns et al. (1998). Di Giacomo et al. (1991) derived an UD diameter of 33 ± 1.3 mas from their lunar occultation measurements (May 1990, cycle+phase of $-7 + 0.2$) in the Br γ line of atomic hydrogen at 2.16 μm. Tej et al. (1999) obtained UD diameters of 39 ± 3 mas and 34 ± 2 mas from their lunar occultation observations through a narrowband filter at 3.36 μm (December 1997, cycle+phase of $2 + 0.17$) and a broadband filter at 2.2 μm (March 1998, cycle+phase of $2 + 0.44$), respectively. K-band observations with the IOTA interferometer by Perrin et al. (1999) yielded UD diameters of 28.18 ± 0.05 mas at cycle+phase of $0 + 0.24$

Fig. 7. Top: Angular Rosseland radii (in mas) derived for each model-phase combination m from the 1045/9 measurements. Middle: Linear Rosseland observed and model radii. The observed linear Rosseland radii were derived for each model-phase combination m from the 1045/9 observations. Bottom: Effective model temperatures for all model-phase combinations m and effective temperatures derived from the above angular Rosseland radii (top) and the the bolometric flux of R Leo measured around phase 0.20. Table 6 gives the link between the abscissa values and the models and their phases (diamonds: observations reduced with model CLVs with phases close to the phase of the observation; crosses:observations reduced with model CLVs with phases far from the phase of the observation; squares: theoretical model values).

(April 17–18, 1996) and 30.68 ± 0.05 mas at cycle+phase of $1 + 0.28$ (March 3–10, 1997). Note that the 1996 measurement of Perrin et al. was done at nearly the same phase of the same pulsation cycle as the here presented observations.

The difference between our 1045 nm/9 nm UD diameter (at cycle+phase of $0 + 0.20$) and the K-Band UD diameter of Perrin et al. (1999; at cycle+phase of $0 + 0.24$) is larger than expected and may indicate that there exists an additional near-infrared extinction, not included in the BSW96 and HSW98 models, which blankets the $1\,\mu$m region more strongly than the K bandpass. No such opacity source is known so far, but Bedding et al. (2001) noticed that dust particles condensating in the uppermost atmospheric layers may produce this type of effect by generating a two-component appearance of the CLV which is more pronounced at shorter λ. Danchi et al. (1994) claim that R Leo belongs to a class of stars whose inner dust-shell radii are very close to the photosphere (3 to 5 photospheric radii), i.e. dust might be formed in the uppermost atmospheric layers. Therefore, we cannot exclude that our measured radius has to be scaled to the true-continuum radius resulting in a smaller stellar radius and in a higher effective temperature. A similar $1\,\mu$m vs. K-band discrepancy was reported for the Mira variable R Cas (Weigelt et al. 2000).

When measured visibility data are reduced with limb-darkening profiles predicted by recent Mira models (BSW96, HSW98), we find that strong-TiO $\tau_\lambda = 1$ diameters depend substantially on the adopted model, whereas the continuum diameter does not. Since these models are taylored to the parameters of o Ceti which has nearly the same period and luminosity as R Leo (310 days, $6540 \pm 3010\,L_\odot$), they should predict also quantitatively the basic properties of R Leo. The predictions of the E model series are in good agreement with (i) the stellar filter radii measured through five of six filters (however, the stellar filter radii measured in the strong TiO absorption band at 673 nm are about 50% larger than the model-predicted values, i.e. the models of the E series as well as the other models considered here are systematically too compact; see Appendix); (ii) the measured Rosseland radius and the derived pulsation mode; and (iii) the measured effective temperature of 2590 K $\pm$ 180 K at near-maximum phase 0.20. We obtain a Rosseland $\tau_{\mathrm{Ross}} = 1$ radius of $R = 417\,R_\odot$ (based on the E-model at phase 1.21 close to the phase of our observations) with an accuracy of about 23% (the error of the HIPPARCOS parallax of $\sim$20% is the largest fraction of the total error; the speckle error is $\sim$10%).

5. Appendix

5.1. Comparison of observed and model diameter ratios

We have also compared the model stellar filter radii $R_{\mathrm{f},m}^t$ as predicted by each model-phase combination m with our measured angular stellar filter radii $R_{\mathrm{f},m}^a$ by comparing the observed and model diameter ratios at different wavelengths (filter f: 656/10, 673/8, 699/6, 754/6, 781/14 and 1045/9). By confronting a large variety of Mira models with the here presented narrow-bandpass observations, we may test how sensitively monochromatic radius measurements probe model structures and whether they are indeed reliable tools of Mira diagnostics. Since different models predict, at different phases, both different stellar filter radii R_{f} and different filter CLV curves, we expect better agreement between model-predicted ratios and observed ratios (based upon the corresponding model-phase combination of CLV) for models that represent R Leo well and for model phases that are close to the observed phases than for other models and phases. Since our five models are taylored to the parameters of o Ceti which roughly has the same period and luminosity as R Leo (310 days, $6540 \pm 3010\,L_\odot$: derived from its bolometric flux measured at phase 0.20 close to our observations and its HIPPARCOS parallax), this comparison should give some hint as to whether any of the models is a fair representation of R Leo. We must be aware, however, that model phases are close to but not identical with observed phases, and cycle-to-cycle variations may be substantial (BSW96, HSW98).

For illustration, Fig. 8 presents the observed and model ratios $R_{\mathrm{f}}/R_{1045\mathrm{nm}}$ of the stellar filter radii R_{f} and $R_{1045\mathrm{nm}}$ as a function of wavelength λ for all applied model series (D, E, P, M and O) and phases close to our observations (since nearly all model series consist of several cycles, a best fit selection was applied). Figure 9 displays the observed and theoretical ratios for all model-phase combinations m and all filter pairs. Figure 10 presents the distance D_m between the measured and model stellar filter radius ratios (between all possible pairs of filters) for each model-phase combination. The distance D_m is defined as

$$D_m := \sqrt{\frac{\sum_{i \neq j}^{N_{\mathrm{f}}} \left| \frac{R_{i,m}}{R_{j,m}} - \frac{R_{i,m}^t}{R_{j,m}^t} \right|^2}{\sum_{i \neq j}^{N_{\mathrm{f}}} \left| \frac{R_{i,m}^t}{R_{j,m}^t} \right|^2}}, \tag{1}$$

where N_{f} is the number of filters used and the filter designation numbers i and j range between 1 and N_{f} (here: $N_{\mathrm{f}} = 6$). The errors of the distances D_m were estimated according to the Gaussian error propagation law.

Inspection of Figs. 8, 9 and 10 shows that from the point of view of diameter ratios, some of the model-phase combinations are acceptable as representations of the here presented observations of R Leo but none is completely satisfactory. Nearly all models are too compact in the strong TiO absorption band at 673 nm, i.e. the distance-independent ratio $(R_{673\mathrm{nm}} - R_{\mathrm{continuum}})/R_{\mathrm{continuum}}$ is too

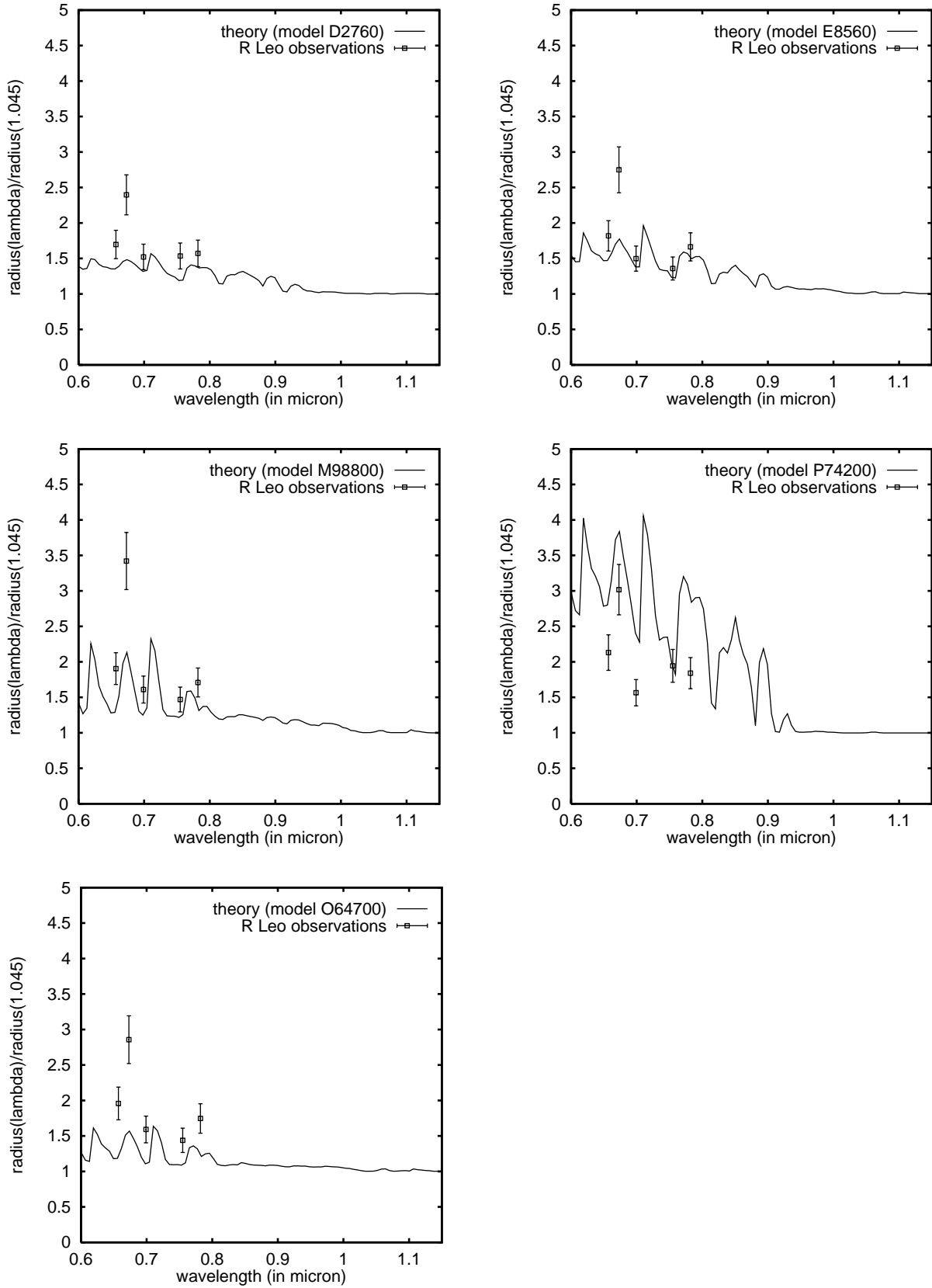**Fig. 8.** Observed and model radius ratios R_f/R_{1045nm} of stellar filter radii R_f and R_{1045nm} as a function of wavelength for all five models and for model phases close to our observations. The plotted theoretical stellar filter radius curve $R_f(\lambda)$ is derived from the monochromatic one by convolution with a rectangular-shaped function with a bandwidth of 6 nm (=bandwidth of our optical filters with the narrowest width).
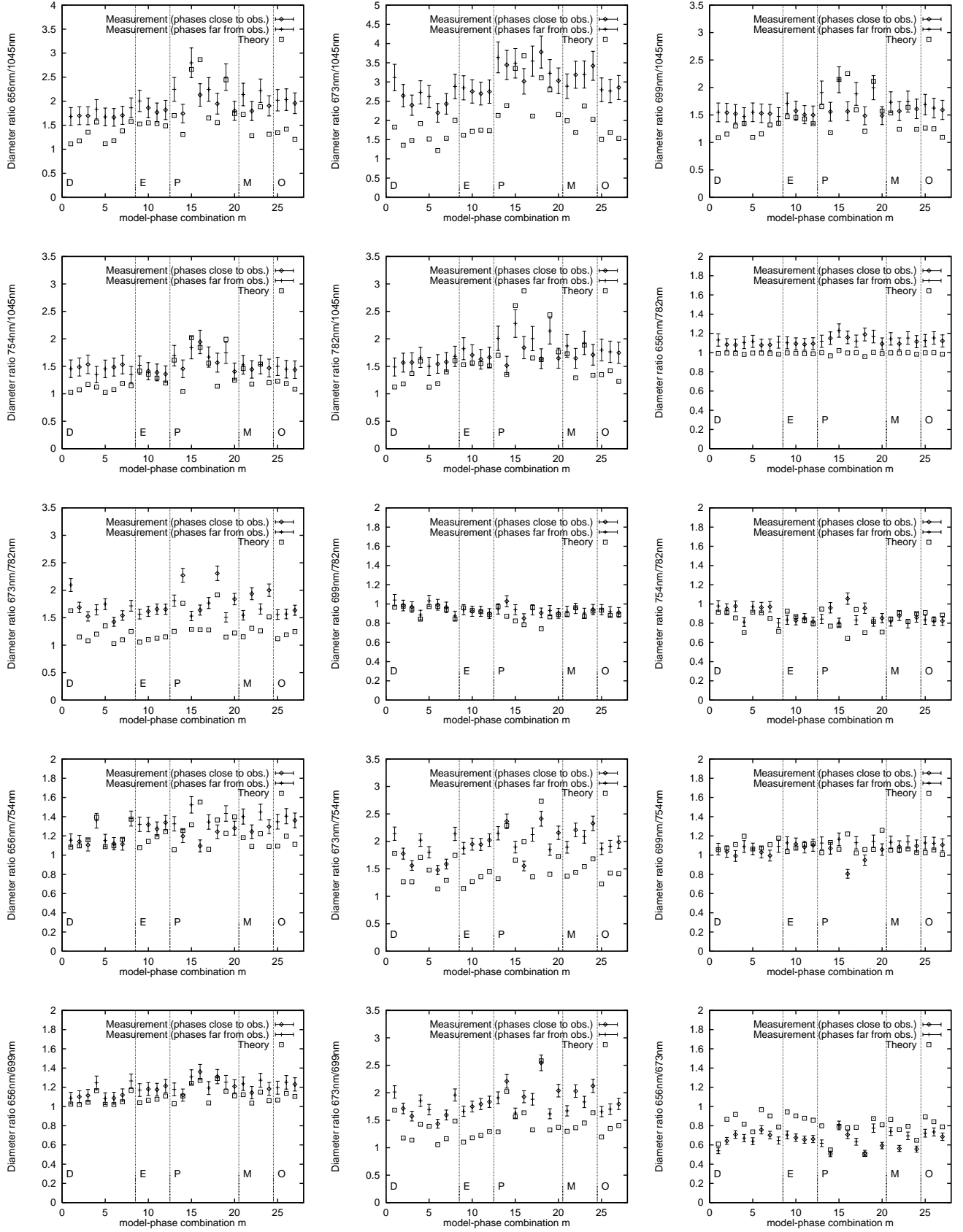
Fig. 9. Observed and model radius ratios R_i/R_j of stellar filter radii R_i and R_j (i and j denote filters). The 15 plots show all possible filter combinations. Table 6 gives the link between the abscissa values and the models and their phases.
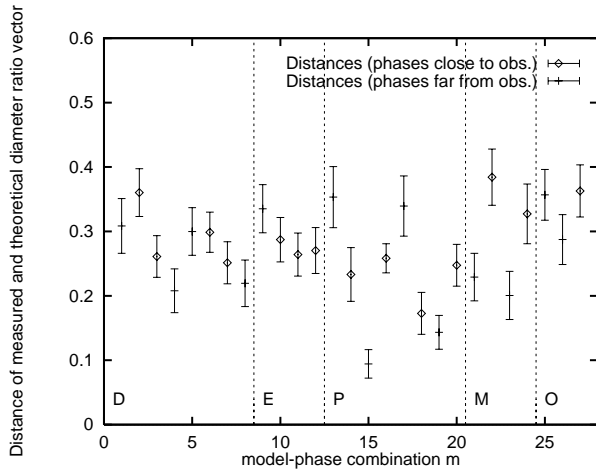
Fig. 10. Normalized distance D_m between measured and model diameter ratio vectors (see text; diamonds: observations reduced with model CLVs with phases close to the phase of the observation; crosses: observations reduced with model CLVs with phases far from the phase of the observation; squares: theoretical model radii). Table 6 gives the link between the abscissa values and the 27 model-phase combinations m.

small compared with the observations. For the model-phase combinations at phases close to the observation, the P model series which exhibits the most pronounced atmospheric extension of the BSW96/HSW98 studies has in most cases (i.e., in 11 out of all 15 filter ratio combinations) model diameter ratios which are identical (within the error bars) to the measured ones. The order of ranking after the P model is: E model (6/15), D model (6/15), M model (3/15) and O model (1/15).

References

Baier, G., & Weigelt, G. 1983, A&A, 121, 137

Bedding, T. R., & Zijlstra, A. A. 1998, ApJ, 506, L47

Bedding, T. R., Jacob, A. P., Scholz, M., & Wood, P. R. 2001, MNRAS, in press

Bessell, M. S., Brett, J. M., Scholz, M., & Wood, P. R. 1989, A&A, 213, 209

Bessell, M. S., Scholz, M., & Wood, P. R. 1996, A&A, 307, 481 (BSW96)

Bonneau, D., & Labeyrie, A. 1973, ApJ, 181, L1

Bonneau, D., Foy, R., Blazit, A., & Labeyrie, A. 1982, A&A, 106, 235

Burns, D., Baldwin, J. E., Boyson, R. C., et al. 1998, MNRAS, 297, 462

Danchi, W. C., Bester, M., Degiacomi, C. G., Greenhill, L. J., & Townes, C. H. 1994, AJ, 107(4), 1469

Di Giacomo, A., Richichi, A., lisi, F., & Calamai, G. 1991, A&A, 249, 397

ESA 1997, The Hipparcos & Tycho Catalog, ESA SP-1200, Noordwijk: ESA

Feast, M. W. 1996, MNRAS, 278, 11

Fluks, M. A., Plez, B., Thé, P. S., et al. 1994, A&AS, 105, 311

Haniff, C. A., Ghez, A. M., Gorham, P. W., et al. 1992, AJ, 103, 1662

Haniff, C. A., Scholz, M., & Tuthill, P. G. 1995, MNRAS, 276, 640

Hofmann, K.-H., & Scholz, M. 1998, A&A, 335, 637 (HS98)

Hofmann, K.-H., & Weigelt, G. 1986, A&A, 167, L15

Hofmann, K.-H., Balega, Y., Scholz, M., & Weigelt, G. 1995a, in Stellar surface structure, IAU Symp. 176, ed. K. G. Strassmeier (Kluwer), Poster Proceedings 45

Hofmann, K.-H., Seggewiss, W., & Weigelt, G. 1995b, A&A, 300, 403

Hofmann, K.-H., Scholz, M., & Wood, P. R. 1998 A&A, 339, 846 (HSW98)

Hofmann, K.-H., Balega, Y., Scholz, M., & Weigelt, G. 2000a, A&A, 353, 1016

Hofmann, K.-H., Beckmann, U., Blöcker, T., et al. 2000b, in Interferometry Optical Astronomy, ed. P. Lena, & A. Quirrenbach, Soc. Photo-Opt. Instr. Eng., 4006, 688

Karovska, M., Nisenson, P., Papaliolios, C., & Boyle, R. P. 1991, ApJ, 374, L51

Labeyrie, A. 1970, A&A, 6, 85

Labeyrie, A., Koechlin, L., Bonneau, D., Blazit, A., & Foy, R. 1977, ApJ, 218, L75

Lattanzi, M. G., Munari, U., Whitelock, P. A., & Feast, M. 1997, ApJ, 485, 328

Lockwood, G. W. 1972, ApJS, 24, 375

Lockwood, G. W., & Wing, R. F. 1971, ApJ, 169, 6

Lohmann, A. W., Weigelt, G., & Wirnitzer, B. 1983, Appl. Opt., 22, 4028

Pease, F. G. 1931, Ergebn. Exacten Naturwiss., 10, 84

Perrin, G., Coudé du Foresto, V., Ridgway, S. T., et al. 1999, A&A, 345, 221

Quirrenbach, A., Mozurkewich, D., Armstrong, J. T., et al. 1992, A&A, 259, L19

Richichi, A., Fabbroni, L., Ragland, S., & Scholz, M. 1999, A&A, 344, 511

Scholz, M. 1985, A&A, 145, 251

Scholz, M., & Takeda, Y. 1987, A&A, 186, 200, erratum: 196, 342

Scholz, M., & Wood, P. R. 2000, A&A, 362, 1065

Tej, A., Chandrasekhar, T., & Ashok, N. M. 1999, AJ, 117, 1857

Tuthill, P. G., Haniff, C. A., & Baldwin, J. E. 1994, in Very high angular resulution imaging, ed. J. G. Robertson, & W. J. Tango (Kluwer, Dordrecht), IAU Symp., 158, 395

Tuthill, P. G., Haniff, C. A., & Baldwin, J. E. 1999, MNRAS, 306, 353

Van Belle, G. T., Dyck, H. M., Benson, J. A., & Lacasse, M. G. 1996, AJ, 112, 2147

Von der Lühe, O. 1984, J. Opt. Soc. Am. A., 1, 510

Watanabe, T., & Kodaira, K. 1979, PASJ, 31, 61

Weigelt, G. P. 1977, Opt. Commun., 21, 55

Weigelt, G., Balega, Y., Hofmann, K. -H., & Scholz, M. 1996, A&A, 316, L21

Weigelt, G., Mourard, D., Abe, L., et al. 2000, in Interferometry in Optical Astronomy, ed. P. Lena, & A. Quirrenbach, Soc. Photo-Opt. Instr. Eng., 4006, 617

Whitelock, P., & Feast, M. 2000, MNRAS, 319, 759

Wilson, R. W., Baldwin, J. E., Buscher, D. F., & Werner, P. J. 1992, MNRAS, 257, 369

Wood, P. R. 1990, in Confrontation between stellar pulsation and evolution, ed. C. Caccari, & G. Clementini, Astronomical Society of the Pacific, San Francisco, California, ASP Conf. Ser., 11, 355

Wood, P. R., MACHO collaboration 1999, in Asymptotic Giant Branch Stars. ed. T. Le Bertre, A. Lèbre, & C. Waelkens, ASP, San Francisco, IAU Symp., 191, 151